AGU PUBLICATIONS

JGR

Journal of Geophysical Research: Oceans

RESEARCH ARTICLE

10.1002/2015JC010790

Sea-surface salinity fronts and associated salinity-minimum zones in the tropical ocean

Lisan Yu[1]

[1]Department of Physical Oceanography, Woods Hole Oceanographic Institution, Woods Hole, Massachusetts, USA

Key Points:
- SSS fronts are associated with salinity-minimum zones (SMZs) of 50–80 m deep
- SMZs are formed by Ekman convergence of the ITCZ-freshened surface waters
- SMZs propagate poleward at a speed of 3.5 km d^{-1} for 12–16 months

Correspondence to:
L. Yu,
lyu@whoi.edu

Citation:
Yu, L. (2015), Sea-surface salinity fronts and associated salinity-minimum zones in the tropical ocean, *J. Geophys. Res. Oceans*, *120*, 4205–4225, doi:10.1002/2015JC010790.

Received 17 FEB 2015
Accepted 13 MAY 2015
Accepted article online 15 MAY 2015
Published online 8 JUN 2015

Abstract The Intertropical Convergence Zone (ITCZ) is a major source of the surface freshwater input to the tropical open ocean. Under the ITCZ, sea-surface salinity (SSS) fronts that extend zonally across the basins are observed by the Aquarius/SAC-D mission and Argo floats. This study examined the evolution and forcing mechanisms of the SSS fronts. It is found that, although the SSS fronts are sourced from the ITCZ-freshened surface waters, the formation, structure, and propagation of these fronts are governed by the trade wind driven Ekman processes. Three features characterize the governing role of Ekman forcing. First, the SSS fronts are associated with near-surface salinity-minimum zones (SMZs) of 50–80 m deep. The SMZs are formed during December–March when the near-equatorial Ekman convergence zone concurs with an equatorward displaced ITCZ. Second, after the formation, the SMZs are carried poleward away at a speed of ~3.5 km d^{-1} by Ekman transport. The monotonic poleward propagation is a sharp contrast to the seasonal north/south oscillation of the ITCZ. Lastly, each SMZ lasts about 12–15 months until dissipated at latitudes beyond 10°N/S. The persistence of more than 1 calendar year allows two SMZs to coexist during the formation season (December–March), with the newly formed SMZ located near the equator while the SMZ that is formed in the previous year located near the latitudes of 10–15° poleward after 1 year's propagation. The contrast between the ITCZ and SMZ highlights the dominance of Ekman dynamics on the relationship between the SSS and the ocean water cycle.

1. Introduction

The tropical rainfall associated with the Intertropical Convergence Zone (ITCZ) is most intense and persistent over the global ocean [*Waliser and Gautier*, 1993; *Xie and Arkin*, 1997; *Adler et al*., 2003]. The high amount of precipitation dominates the tropical hydrological cycle [*Betts and Ridgway*, 1989; *Allen and Ingram*, 2002] and leads to the formation of low-salinity waters at the surface [*Fiedler and Talley*, 2006; *Johnson et al*., 2012] that affects the dynamics and thermodynamics in the tropical ocean [e.g., *Lukas*, 1990; *Maes et al*., 2006; *Johnson et al*., 2012]. Formation of the salinity-stratified temperature mixed layer [*Godfrey and Lindstrom*, 1989; *Lindstrom*, 1991] is evidenced at many locales, and is credited for regulating the tropical air-sea exchange of heat, moisture, and momentum, and modulating the atmosphere-ocean coupling on time scales ranging from diurnal to interannual [e.g., *Delcroix and Henin*, 1991; *Vialard and Delecluse*, 1998]. In recent years, surface and subsurface salinity observations are made available from the Argo network of autonomous profiling floats [*Roemmich et al*., 2009] and satellite salinity missions that include the Aquarius/SAC-D by NASA [*Lagerloef et al*., 2008] and the SMOS by the European Satellite Agency [*Font et al*., 2010; *Reul et al*., 2014]. The rapid augment of the global salinity database has fueled the long-held interest in using ocean salinity as a rain gauge to detect the change of the global hydrological cycle [*Elliott*, 1974].

Freshwater is a mass flux. When added to the ocean surface, it introduces oceanic adjustments on various temporal and spatial scales. *Brainerd and Gregg* [1997] noticed that the tropical rainfall is often very intense and very localized in space and time, occurring in squalls with length scales from 2 to 50 km [e.g., *Short et al*., 1997]. After heavy rainfall, a shallow puddle with low salinity and low temperature usually forms at the surface [*Wijesekera et al*., 1999; *Asher et al*., 2014], producing a density-depression anomaly, and thus a density gradient, that tends to spread as gravity currents in the horizontal direction [*Simpson and Britter*, 1979]. The gravity currents can generate different modes of internal waves, and the resonant coupling between the gravity currents and internal waves lead to a series of frontal interfaces. *Soloviev et al*. [2002] suggested that, depending on the atmospheric forcing conditions in the tropics, the frontal interfaces may

either evolve into a bore-like structure that intensifies the cross-frontal exchange and leads to the elimination of the interface, or become an arrested wedge in which the interface reaches a compensated state (i.e., the cross-frontal difference in temperature is compensated by that in salinity) and freezes the frontal structure. *Soloviev and Lukas* [1997] speculated that the direction of the wind stress relative to the density gradient of the frontal interface is a factor in determining the fate of the frontal evolution. Frontal interfaces, of less than 100 m width, were frequently observed during the TOGA COARE [*Soloviev and Lukas*, 1997; *Wijesekera et al*., 1999].

The evolution of the fine-scale front generated by a rain squall cannot be detected by the Aquarius sensor that has a smallest footprint of 60 × 90 km and the swatch width of 390 km [*Lagerloef et al*., 2008]. Nevertheless, the cumulative effect of the multitudinous rain squalls in the ITCZ region could be substantial over time and influence the surface salinity structures on weekly and monthly time scales. Zonally oriented, basin-scale SSS fronts are a dominant feature in the Aquarius sea-surface salinity (SSS) observations of the tropical ocean [*Kao and Lagerloef*, 2015], with the longest one extending across the north tropical Pacific at latitudes between 2°N and 10°N [*Yu*, 2014]. Conventionally, a salinity front represents the convergence of two water masses with different salinities. Given the close proximity of the SSS fronts to the ITCZ, there is no doubt that these fronts are an expression of the interaction between the ITCZ-generated fresher surface waters and the ambient saltier surface waters. Since salinity is a conservative tracer, the ITCZ rainfall information embedded within the SSS fronts is potentially inferable from the salinity observations.

Given the potential linkage of the tropical SSS fronts to the tropical water cycle, there is a need for a better understanding of the SSS fronts regarding, in particular, the evolution and forcing mechanisms. Thus, as the first step toward ascertaining the structure and dynamics of the SSS fronts, the author in a recent study [*Yu*, 2014] conducted a focused analysis on the tropical north Pacific that features the longest SSS front among all the basins. The analysis yielded an important finding that the SSS front is not a stand-alone feature but a surface manifestation of the salinity-minimum zone (SMZ) that exists in the upper 50–80 m. The analysis also obtained that although the SMZ is sourced from the ITCZ rainfall, the generation and distribution of the SMZ are strongly controlled by the wind-driven Ekman processes. One feature is outstanding: the SMZ has a monotonic northward progression that differs sharply from the seasonal north-south oscillation of the ITCZ.

SSS fronts are present in all tropical basins [*Kao and Lagerloef*, 2015]. If the findings of *Yu* [2014] are robust, there should be a SMZ corresponding to each SSS front because the forcing conditions are similar across the ITCZ rain band. Hence, the main objective of the study is to investigate the intertropical context of the SMZ and to assess the generality of the findings of *Yu* [2014] for the tropical ocean as a whole. By building on and extending the initial work in the tropical Pacific [e.g., *Donguy and Henin*, 1980; *Delcroix et al*., 1996; *Johnson et al*., 2002; *Yu*, 2011, 2014; *Hasson et al*., 2013], the study aims to generalize and document the main characteristics of the SSS fronts/SMZ and to provide a comprehensive view on the leading forcing mechanisms of the intertropical SMZ. In particular, a better insight has been gained into the relative roles in the temporal and spatial distribution of the SMZs since the publication of *Yu* [2014]. This is a time to revise, expand, and bring the knowledge up to date.

The presentation is organized as follows: section 2 provides a brief description of the data sets and the analysis approach used in the study. Section 3 presents the analysis of the annual-mean state of the surface salinity-minimum waters, the coupling between the SSS fronts and the subsurface structure, and the relationship between the salinity-minimum waters and the ITCZ precipitation. The seasonal variability of the SMZ is presented in section 4, and the mechanisms governing the generation and movement of the SMZ are discussed in section 5. Summary of the results and discussion of the potential implications of the SMZ for the tropical water cycle are given in section 6.

2. Data and Method

2.1. Salinity Observations

Two sets of salinity observations were used: the Aquarius SSS and the Argo subsurface salinity fields both gridded on 1° boxes. Aquarius/SAC-D is a combined passive/active L-band microwave instrument developed to map the salinity field at the surface of the ocean from space [*Lagerloef et al*., 2008], and has been operating since 25 August 2011 aboard the Argentine SAC-D spacecraft. Since then, the sensor has

generated near-synoptic global views of SSS for more than 3 years with a 7 day repeat cycle. The primary science objective of the Aquarius mission is to monitor the seasonal and interannual variation of the large-scale features of the global SSS field with a spatial resolution of 150 km and a retrieval accuracy of 0.2 Practical Salinity Scale 1978 (PSS-78) on a monthly basis. The Aquarius SSS product used here was taken from the Level-2 Combined Active-Passive (CAP) version 3.0 product [*Yueh et al*., 2014]. The CAP algorithm simultaneously retrieves salinity, wind speed, and wind direction from Aquarius' brightness temperature and radar backscatter by minimizing the sum of squared differences between the model and observations. A mean seasonal cycle was constructed from the 2 full years of the Aquarius observations between January 2012 and December 2013.

The Argo network of autonomous profiling floats provides in situ salinity profiles over the global ocean through the deployment of over 3000 free-drifting profiling floats that measure salinity and temperature from near the surface to 2000 dbar [*Roemmich et al*., 2009]. We used the monthly gridded Argo data product from the Japan Agency for Marine-Earth Science and Technology (JAMSTEC) [*Hosoda et al*., 2010], which is constructed from optimal interpolation (OI) of ARGO floats, Triangle Trans-Ocean Buoy Network (TRITON), and available conductivity-temperature-depth (CTD) casts. The salinity fields are gridded onto 1° grids horizontally, and 25 pressure levels from 2000 to 10 dbar below the surface. We used the salinity of the surface mixed layer rather than the salinity at 5 db when comparing with the Aquarius SSS. The mixed-layer depth (h) was computed from the monthly temperature and salinity fields based on a density criterion, i.e., h is determined as the depth at which density is 0.125 kg m^{-3} higher than the surface density [*de Boyer Montégut et al*., 2004]. Two sets of seasonal cycle climatology were constructed. One was based on the 10 year Argo observing period from 2004 to 2013 and the other based on the 2 year Aquarius period from 2012 to 2013. The differences between the two sets of seasonal cycle climatology are small.

2.2. The Salinity Budget Equation

A data-based salinity budget analysis was conducted to help diagnose the dominant forcing for the seasonal change of the near-surface salinity. Following *Mignot and Frankignoul* [2003], the equation for the MLS can be expressed as [*Yu*, 2011]:

$$\frac{\partial S'}{\partial t} \approx \frac{S_0(E'-P')}{\bar{h}} - \bar{\mathbf{U}} \cdot \nabla S' - \mathbf{U}' \cdot \nabla \bar{S} - \frac{(\Gamma(w_e)(S-S_b))'}{\bar{h}} + \kappa \nabla^2 S' \tag{1}$$

where an overbar denotes the mean and a prime denotes the departure from the mean, S the MLS, S_0 the mean surface salinity, E evaporation, P precipitation, h the mixed-layer depth, $\boldsymbol{U}$ the horizontal transport in the mixed layer and positive to the east and north, w_e is the entrainment velocity at depth $z = h$, S_b the salinity chosen as the salinity 20 m below the mixed layer depth h, Γ the Heaviside function, and κ the horizontal mixing coefficient set to 500 m s^{-2}. The Heaviside function Γ is introduced to represent the different effects of the entrainment ($w_e > 0$) and detrainment ($w_e < 0$) on the MLS. The entrainment of subsurface stratified water affects the MLS whereas the detrainment of the mixed layer water into the subsurface does not change the MLS [*Kraus and Turner*, 1967].

The horizontal transport $\boldsymbol{U}$ in equation (1) includes two components, the wind-driven Ekman component $\boldsymbol{U}_{EK}$ and the geostrophic component $\boldsymbol{U}_g$, and can be expressed as:

$$\boldsymbol{U} = \boldsymbol{U}_{EK} + \boldsymbol{U}_g = \frac{\boldsymbol{\tau} \times \boldsymbol{k}}{\rho f} + \frac{hg \nabla \eta \times \boldsymbol{k}}{f} \tag{2}$$

where τ denotes wind stress, g the gravity acceleration, f the Coriolis frequency, and η the sea-surface elevation.

The entrainment velocity w_e in equation (1) consists of vertical Ekman velocity W_{EK} and the h tendency:

$$w_e = w_{EK} + \left(\frac{\partial h}{\partial t} + \nabla \cdot h\boldsymbol{U}\right) = \frac{\nabla \times \boldsymbol{\tau}}{\rho f} + \left(\frac{\partial h}{\partial t} + \nabla \cdot h\boldsymbol{U}\right) \tag{3}$$

The Ekman vertical velocity W_{EK} corresponds to the upwelling/downwelling generated by the convergence/divergence of the horizontal Ekman transport. The h tendency term represents the integrated effects of wind, surface buoyancy flux, and turbulent dissipation on the change of the mixed-layer depth [*Niiler and Kraus*, 1977].

Substituting equation (2) into equation (1) yields the following MLS equation:

$$\frac{\partial S'}{\partial t} \approx \frac{S_0(E'-P')}{\bar{h}} - \bar{\mathbf{U}}_{\boldsymbol{EK}} \cdot \nabla S' - \mathbf{U}'_{\boldsymbol{EK}} \cdot \nabla \bar{S} - \bar{\mathbf{U}}_{\boldsymbol{g}} \cdot \nabla S' - \mathbf{U}'_{\boldsymbol{g}} \cdot \nabla \bar{S} - \frac{(\Gamma(w_e)(S-S_b))'}{\bar{h}} + \kappa \nabla^2 S' \quad (4)$$

The left-hand side denotes the rate of change of the MLS (or the MLS tendency), while on the right-hand side, the first term denotes the effective surface E-P forcing, the second term is the advection of the anomalous MLS gradient by mean Ekman currents, the third is the advection of the mean MLS gradient by anomalous Ekman currents, the fourth term is the advection of the MLS by mean geostrophic currents, the fifth term is the advection of the MLS by anomalous geostrophic currents, the sixth term is the entrainment/detrainment of the MLS through the base of the mixed layer, and the last term represents horizontal mixing.

The computation of equation (4) requires three surface forcing data sets, precipitation (*P*), evaporation (*E*), and surface wind stress (τ). The *P* data set was the 0.25° gridded multisatellite precipitation analysis 3B43 product (version 7), merged from the Tropical Rainfall Measuring Mission (TRMM) and precipitation estimates from other satellites [*Hoffman et al*., 2007]. The data set is available from January 1998 to the present. The *E* data set was taken from Version 3 products of the Objectively Analyzed air-sea Fluxes (OAFlux) project [*Yu and Weller*, 2007; *Yu et al*., 2008]. The OAFlux 1° gridded analysis covers the period from January 1958 onward. The wind stress data set was taken from the OAFlux satellite-based, 0.25° gridded, daily global vector wind analysis developed from merging 14 satellite sensors for the period of 1987 onward [*Yu and Jin*, 2014]. The Ekman transport ($\boldsymbol{U}_{EK}$) and vertical velocity (W_{EK}) are determined from the wind stress and wind stress curl. The geostrophic component ($\boldsymbol{Ug}$; equation (2)) is computed from two data sets. One is the time-averaged global mean sea-surface height constructed by *Niiler et al*. [2003] and *Maximenko et al*. [2009] to estimate the mean geostrophic component ($\bar{\boldsymbol{U}}_{\boldsymbol{g}}$), and the other data set is the altimeter sea-surface height from AVISO (http://www.aviso.oceanobs.com/es/data/index.htm) to estimate the geostrophic current anomalies ($\boldsymbol{U}'_{\boldsymbol{g}}$). All 0.25° data sets were processed onto the same 1° grid boxes as the salinity products before computing the salinity budget equation (4).

3. Mean Patterns

3.1. Mean Surface Salinity and Precipitation

The precipitation pattern in the tropical ocean is dictated by the narrow east-west rainfall band associated with the ITCZ [*Hastenrath and Lamb*, 1978; *Waliser and Gautier*, 1993]. The mean precipitation field in Figure 1a was an average of the 12 year period from January 2004 to December 2013, the same time frame as the Argo observations. Over the warm pool of the western tropical Pacific, the southeast trending branch of the ITCZ, known as the South Pacific Convergence Zone (SPCZ) [*Vincent*, 1994], stretches from the equatorial region near New Guinea to the South Pacific near 30°S and 120°W. Along the ITCZ rain band, the annual rain accumulation is greater than 300 cm, with a maximum amount of 400 cm occurring in the western tropical Pacific warm pool. In the following discussions, the location line of the rainfall maxima (hereafter *Pmax*) is used to represent the center alignment of the ITCZ/SPCZ rain bands.

The Aquarius observations have a clear depiction of the rain-generated low-salinity water pools in the tropical oceans (Figure 1b). The surface waters with SSS lower than 33 PSS-78 are featured in two major regions. One is the so-called far-eastern Pacific fresh pool [*Donguy and Henin*, 1980; *Delcroix et al*., 2011; *Alory et al*., 2012], which extends northwestward from the coast off Panama to about 120°W. The other fresh pool collocates with the Indo-Pacific warm pool, which constitutes the Bay of Bengal, the eastern tropical Indian Ocean, and the western tropical Pacific. Very low-salinity surface waters (<33 PSS-78) are also featured in the seas marginal to the east and southeast Asia. Similar to the SSS in the Bay of Bengal [*Rao and Sivakumar*, 2003], the SSS in the Asia marginal seas are influenced not only by rainfall but also by continental runoffs and salt transport by ocean currents [*Qu et al*., 2000; *Zeng et al*., 2014]. Since the focus of the present study is on the relationship between the surface low-salinity waters and the ITCZ rainfall, we define the scope of the analysis to the salinity in the open ocean and steer away from the direct influence of continental runoffs.

Within the tropical domain of interest, the surface waters in the tropical Atlantic are saltier than their Pacific counterparts by about 2 PSS-78. Despite the interbasin difference in the absolute values, both the Atlantic

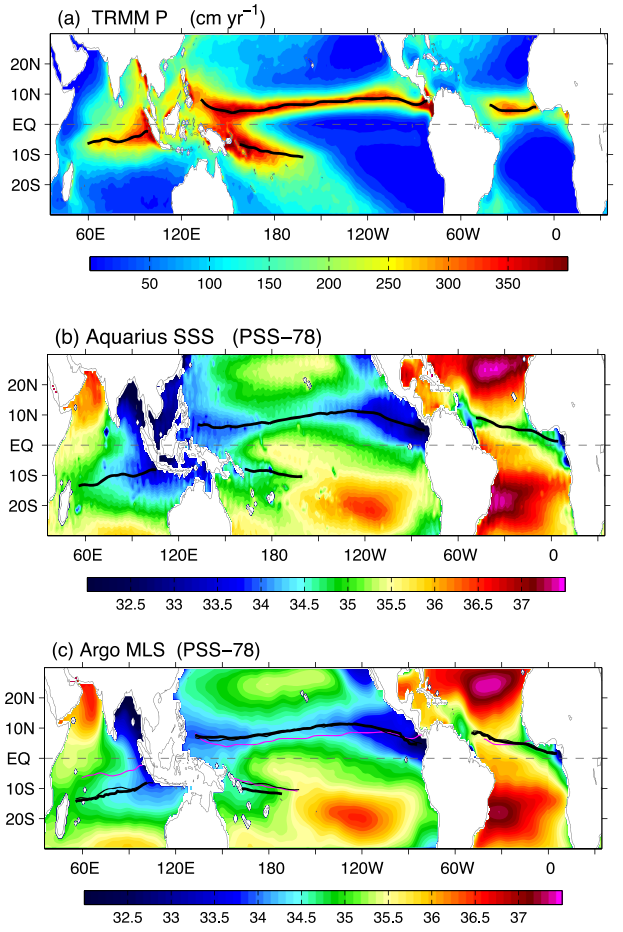

Figure 1. (a) TRMM mean precipitation superimposed with the *Pmax* location line (thick black). (b) Aquarius SSS averaged between January 2012 and December 2013 superimposed with the *Smin* location line (thick black). (c) Argo mixed-layer salinity superimposed with the *Smin* location line (thick black). For comparison, the location lines of the Aquarius *Smin* (thin black) and TRMM *Pmax* (thick magenta) are also superimposed. The TRMM precipitation in Figure 1a and Argo salinity in Figure 1c were constructed for the 12 year period from January 2004 to December 2013.

and Pacific have the similar meridional SSS structure, showing a distinct contrast between the fresher tropical and saltier subtropical oceans. The band of SSS waters lower than 35 PSS-78 lies across the Atlantic equatorial basin in a northwest-southeast direction, and connects with the Amazon freshwater tongue in the west and the freshwater pool of the Gulf of Guinea in the east, with the effects of the Congo and Cameroon river runoff [*Da-Allada et al.*, 2013] particularly noticed off the coast of Africa.

To be consistent with the use of the *Pmax* location line to represent the ITCZ rain bands, the locations of the salinity minima (hereafter *Smin*) are extracted to characterize the center of the distribution of the low-salinity surface waters (Figure 1b). Four *Smin* location lines are identified, one each in the following basins: the south Indian Ocean between 15°S and 5°S, the tropical north Pacific between 5°N and 10°N, the southwest Pacific near 10°S, and the tropical north Atlantic between 2°N and 10°N. We were aware that these locations were extracted from the Aquarius observations of 2 years (2012–2013), and hence introduced the MLS from the 10 year (2004–2013) Argo observations to evaluate the climatological representation of the Aquarius fields (Figure 1c). Interestingly, the Aquarius and Argo observations yielded nearly identical *Smin* locations in all basins except for the southwest Pacific, where the location line of the Argo MLS minima (hereafter *MLSmin*) is shorter and slightly more southward. One explanation is the likely effect of the moderate El Niño in 2012 on the 2 year mean Aquarius field. *Hasson et al.* [2014] indicated that the ENSO signature in SSS is mainly located in the western half of the tropical Pacific Ocean. During an El Niño, a northeastward displacement of the SPCZ is featured and a corresponding northward displacement of the fresher surface waters is also noted [*Gouriou and Delcroix*, 2002]. Despite the influence of interannual variability, the overall good agreement between the *Smin* and the *MLSmin* location lines justifies the climatological representation of the salinity features derived from the Aquarius observations.

The superimposition of the *Pmax* locations onto the MLS annual-mean field (Figure 1c) shows that the *Smin* and *Pmax* location lines are close to each other but do not overlap. The *Smin* are located about 2–3° poleward away from the *Pmax* in the Pacific and Atlantic Oceans, and 7–8° away in the south Indian Ocean. The separation between the *Pmax* and *Smin* locations indicates that the ITCZ rainfall could not be the only forcing that governs the spatial distribution of the low-salinity surface waters.

3.2. SSS Fronts and the *Smin* Locations

The magnitude of the SSS gradient is defined as $\nabla SSS = \sqrt{\left(\partial S/\partial x\right)^2 + \left(\partial S/\partial y\right)^2}$, where $\partial S/\partial x$ and $\partial S/\partial y$ denote the gradient in the zonal and meridional directions, respectively. In the tropical ocean, the spatial

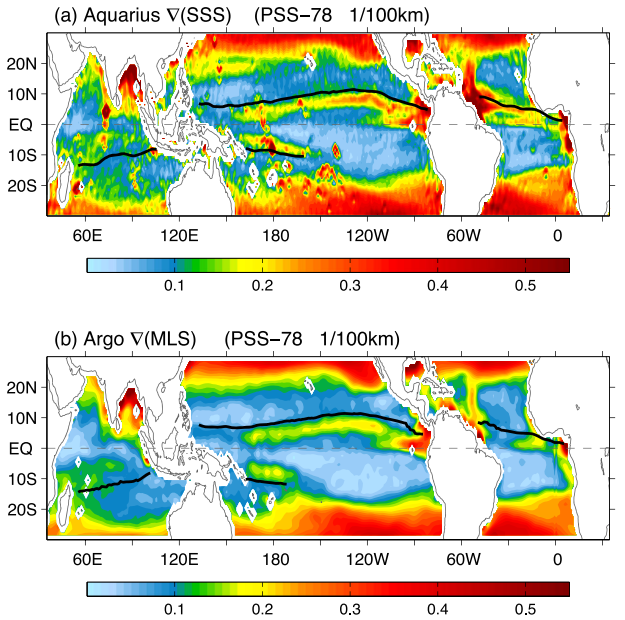

Figure 2. Magnitude of the surface salinity gradients constructed from (a) Aquarius SSS and (b) Argo MLS superimposed with the respective *Smin* location line (thick black).

structure of the surface salinity varies more substantially in the north-south direction than in the east-west direction. *Yu* [2011] showed that the magnitude of the mean $\partial S/\partial y$ is about one order larger than the magnitude of the mean $\partial S/\partial x$ and hence, the ∇SSS field is dominated by the meridional gradient. The surface salinity gradients were computed using both Aquarius and Argo observations (Figures 2a and 2b). The Aquarius ∇SSS field (Figure 2a) features strong SSS fronts oriented near the ITCZ/SPCZ rain bands in all three basins, with the magnitude and zonal scale of the fronts varying with the basin. The SSS front in the north tropical Pacific is longest, lying across the basin from the near-equatorial position at 150°E to the northernmost latitude of ~10°N at 120°W. The front in the southwest tropical Pacific has a shorter zonal scale, extending southeastward from the western Pacific warm pool to the center basin near 160°W, 10°S. The front in the north tropical Atlantic has a better-defined structure in the central basin, but is broadened and enhanced in the west due to the influence of the Amazon river runoff. The front in the South Indian Ocean is the least structured one, with a loosely organized pattern and a weak magnitude.

The zonal alignment and scale of the SSS fronts resemble those of the *Smin* location lines (Figure 1). Indeed, when superimposing the *Smin* location lines onto the Aquarius SSS gradient field (Figure 2a), one striking feature is displayed: the salinity-minimum waters are located on the northern edges of the fronts in the northern hemisphere, and meanwhile on the southern edges of the fronts in the southern hemisphere. In other words, the *Smin* exist on the poleward edges of the SSS fronts. Interestingly, although the SSS fronts are in the vicinity of the ITCZ/SPCZ rain bands, there is no clear relationship between the *Pmax* and *Smin* location lines (Figure 1c).

To validate the representation of the location correlations derived from the Aquarius observations, the same plot is made using the 10 year mean Argo MLS field (Figure 2b). The MLS fronts are broader and weaker, likely due to the coarse nominal spatial sampling resolution (i.e., $3^\circ \times 3^\circ$) of the Argo observations. Despite the difference in resolution, the existence of the *Smin* on the poleward edges of the SSS fronts is consistent between the Aquarius and Argo observations. This well-organized and well-structured collocation pattern is a strong indication that the spatial distribution of the salinity-minimum waters has to be sustained by a common ocean dynamical process.

3.3. SSS Fronts and the SMZ

Yu [2014] showed that the SSS front in the north tropical Pacific is the surface manifestation of a low-salinity zone that exists in the upper 100 m. As the SSS fronts in the tropical basins all have the same surface signature, it would not be a surprise that such surface and subsurface coupling is the cause of every SSS front. Indeed, the Argo subsurface salinity observations reveal that a SMZ is associated with every SSS front in all tropical basins. To characterize the vertical salinity structure of the SMZ, the meridional-depth section plots are made at four locations (Figures 3a–3d): the central Pacific at 140°W, the western Pacific at 170°E, the central Indian Ocean at 70°E, and the central Atlantic at 30°W.

Yu [2014] used the two Pacific locations at 140°W and 170°E but for the portion north of the equator. The expansion of the two sections southward to 25°S allows the comparison of the subsurface structures

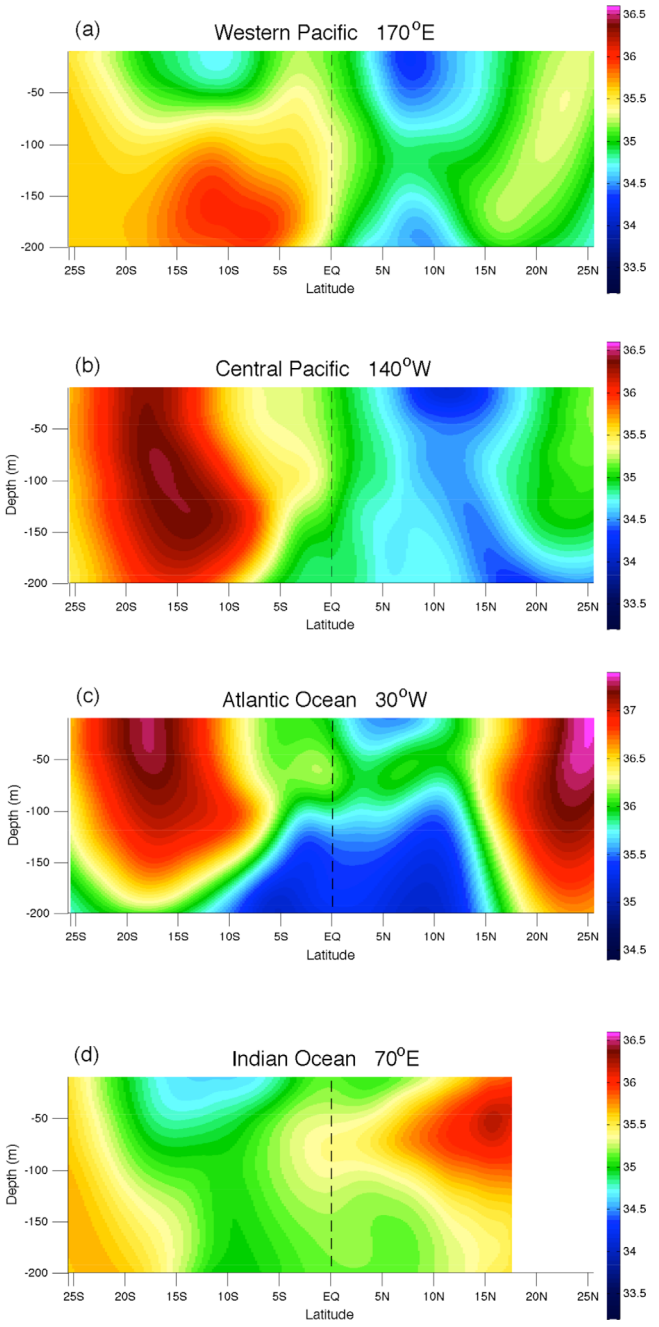

Figure 3. The meridional salinity sections [25°S–25°N] in the upper 200 m at (a) 170°E, (b) 140°W, (c) 30°W, and (d) 70°E.

associated with and without a SSS front in the south tropical Pacific. The western section at 170°E (Figure 3a) features two low-salinity cells in the upper 100 m, with one centered south of the equator around 12°S in the vicinity of the SPCZ, and the other centered north of the equator around 7°N in the vicinity of the ITCZ. The northern cell is fresher (<34.5 PSS-78) and deeper (~80 m) than the southern cell, and they both appear to locate more poleward than the SSS fronts because the central positions of the cells are on the poleward sides of the corresponding SSS fronts (Figure 2a). On the other hand, the central Pacific section at 140°W (Figure 3b) has only one shallow (~50 m) low-salinity (<34.5 PSS-78) cell in the north, consistent with the existence of one salinity front at the surface. At this latitude, the source of the low-salinity waters in the cell should come from the nearby ITCZ. South of the equator, no SSS front is in sight and the subsurface section has a deep high-salinity cell. The contrast in the salinity vertical structure on the two sides of the equator underlines the importance of the surface-subsurface coupling in sustaining the salinity front at the surface.

The meridional sections in the Atlantic (Figure 3c) and central Indian (Figure 3d) Oceans present a similar pattern: a near-surface low-salinity cell exists under each SSS front. Thus, the finding of *Yu* [2014] in the north tropical Pacific is applicable to the entire tropical ocean: the zonally oriented, basin-scale SSS fronts are a good surface indicator of the near-surface SMZ of the tropical ocean. Nevertheless, the vertical sections at the selected locations offer only limited slices of insight into the subsurface structure of the SSS fronts. To gain an integrated view of the horizontal and vertical extents of the SMZ, the basin-scale salinity fields need to be examined in the context of the 3-D space.

We use here the salinity 3-D fields of the upper 100 m in the north tropical Pacific as a focal point for illustration (Figures 4a and 4b). The horizontal domain ranges from 130°E in the west to 85°W in the east, and the domain's northern boundary is set at 25°N. We intend to set the southern boundary at two different locations to compare the vertical cross section outside of the SMZ with the cross section that is in the core of the SMZ. Hence, the southern boundary is fixed at the equator in the first depiction (Figure 4a) and set along the *Smin* location line in the second depiction (Figure 4b).

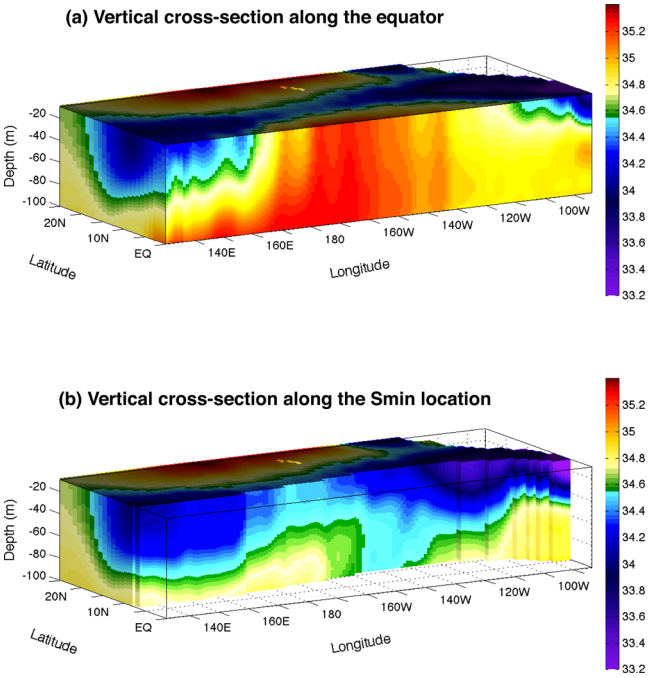

Figure 4. The upper 100 m vertical cross section of mean salinity in the north tropical Pacific with the southern boundary set (a) at the equator, and (b) along the varying *Smin* location line. The northern boundary is fixed at 25°N.

The salinity vertical cross section along the equator (Figure 4a) indicates that salty waters (>35 PSS-78), presumably advected by the south equatorial currents from the subtropical origin [*Qu et al*., 2013], dominates the entire upper 100 m in the central equatorial basin. Fresher waters (<34 PSS-78) of <50 m deep are observed in both the eastern (east of 110°W) and western (west of 170°E) equatorial regions. In the literature, the two freshwater pools are named the eastern fresh pool [*Alory et al*., 2012] and the western equatorial Pacific fresh pool [*Delcroix and Picaut*, 1998], respectively. It is evidenced from the 3-D plot that the two commonly known freshwater pools are part of the SMZ that lies across the basin.

The SMZ in the central Pacific appears to be narrower and less fresh compared to the zone in the eastern and western Pacific. The basin-wide variation of the zone's vertical extent is best seen from the vertical cross section along the *Smin* location line (Figure 4b). The zone is deepest (~80 m) in the western pool, freshest (<33.4) in the eastern pool, and shallowest and least fresh in the central Pacific slightly east of the dateline. The *Smin* locations shift northeastward from the near-equatorial position at 150°E to the northernmost latitude of ~10°N at 120°W, and then turns back toward the equator to the east of 120°W.

4. Seasonal Relationships

4.1. Mismatch Between the *Pmax* and *Smin* Locations

The ITCZ is known for its marked north-south migration with the seasons, moving poleward during the hemisphere's winter months and equatorward during the hemisphere's summer months. It was reported in *Yu* [2014] that the *Smin* location lines do not always collocate with the *Pmax* throughout the year in the northern Pacific. Take SSS and *P* in the western Pacific along the meridian at 175°E as an example (Figure 5a). The distributions of SSS and *P* in February and August are depicted to characterize the changes in winter and summer. Consistent with the classic picture of the ITCZ movement, the *Pmax* has a northward shift from 3°N in February to 5°N in August. A seasonal shift of the *Smin* is also observed, but in a direction different from the *Pmax*. While the *Smin* is located near the *Pmax* at ~5°N in August, it stays far northward at the latitude ~8°N in February when the *Pmax* is near the equator.

The comparison of the *Smin* and *Pmax* locations at other meridional sections verifies that there is a complex *Smin-Pmax* relationship during the hemispheric winter season at all sections. For instance, in the eastern Pacific at 120°W (Figure 5b), the *Smin* at ~10°N corresponds directly with the local *Pmax* in August. Such direct correspondence cannot be found in February. While the *Pmax* is at ~ 7°N, there are two *Smin* locations, with one at ~4°N and the other at ~15°N. The double *Smin* locations in response to one *Pmax* are also observed for the section in the central Atlantic at 30°W in February (Figure 5c). However, in the south Indian Ocean at 65°E (Figure 5d), there are no double *Smin* locations in the winter season (July). The *Smin-Pmax* relationship is similar to the relationship shown in the western Pacific at 175°E (Figure 5d), that is, the *Smin* and *Pmax* collocate in the summer season (January) and separate in the winter season (July) with *Pmax* located at 3°S and *Smin* far southward at ~14°S. In the southwestern Pacific under the influence of the SPCZ (Figure 5f), the *Smin* is not aligned with *Pmax* in either August (winter) or

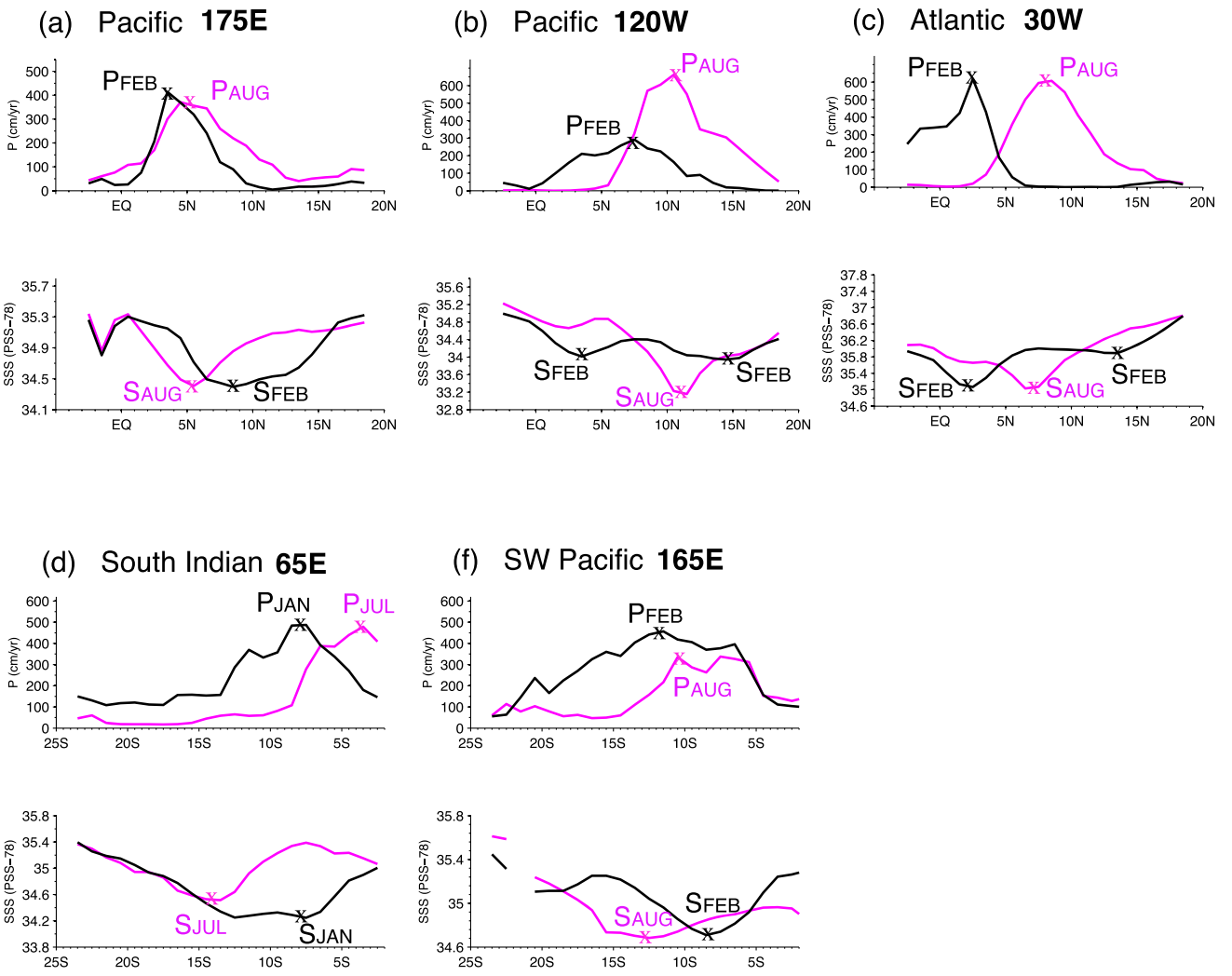

Figure 5. Seasonal relationship between *Pmax* and *Smin* along the meridians at (a) 175°E, (b) 120°W, (c) 30°W, (d) 65°E, and (f) 165°E. For all subplots except for (d), the top plot is the precipitation (P) in February (black) and August (magenta), and the bottom plot is the SSS in February (black) and August (magenta). In Figure 5d, (top) the precipitation and (bottom) SSS are plotted for January (black) and July (magenta).

February (summer). Nevertheless, the *Smin* shows a southward movement when the SPCZ moves northward from February to August.

4.2. Seasonal Migration of the SMZ

To find out how and why the seasonal migration pattern of the *Smin* differs from the seasonal movement of the ITCZ, we first map out the bimonthly evolution of the SSS gradients with the *Smin* locations superimposed (Figure 6). Similar to what has been seen in the annual-mean field (Figure 2), the *Smin* location lines stay on the poleward edges of the SSS fronts for all months. These location lines help to better define the movement of the SMZ amid the noisy gradient fields. In the north tropical Pacific and Atlantic, multiple SSS fronts are observed in some months. For instance, the February field shows two major SSS fronts, with one near the equator and the other near 10°N. The front near the equator strengthens and moves northward in the months that follow. This is seen that in April, the near-equatorial front enhances and expands westward. In June, the front further enhances while moving a few degrees northward away from the equator. The front arrives at the latitudes between 5°N and 8°N in August and remains at the same position in October, during which the front's magnitude is boosted considerably. In December, the front is noticeably weakened and also northward shifted compared to its condition in October. The front continues its northward movement for a few more months in the following year, located near 10°N in February and beyond 10°N in April.

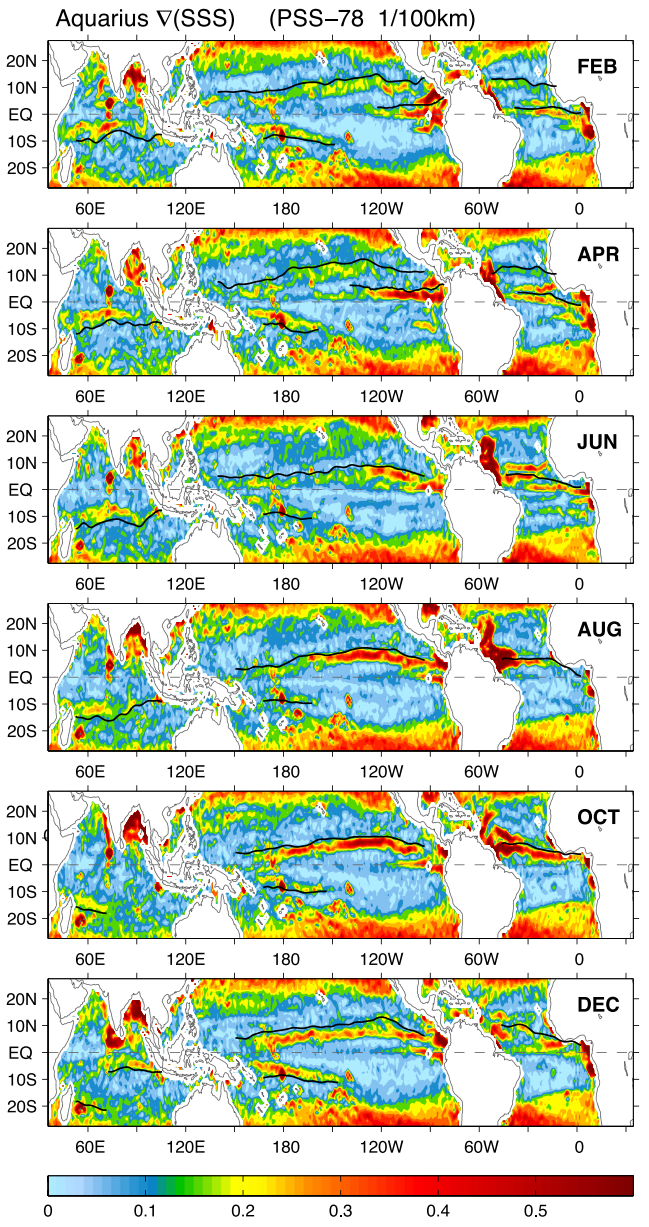

Figure 6. Bimonthly evolution of the surface salinity gradient fields from (top) February to (bottom) December superimposed with the *Smin* location lines (black lines).

The front dissipates in June, leaving behind a trail of weak and fractured SSS gradients near 15°N. It appears that the existence of two major SSS fronts in February and April is a result of two concurring processes: the generation of a new SSS front near the equator and the northward propagation of the SSS front that is generated in the previous year.

The seasonal migration pattern of the SSS fronts in the north tropical Atlantic mirrors the pattern in the north tropical Pacific, that is, the two SSS fronts observed in February and April are due to the existence of one new and one old front. The new SSS front being developed near the equator propagates northward in the months that follow, and turns into the SSS front that is located at 10°N for the following spring. In the north tropical Pacific and Atlantic, the SSS front persists about 15–16 months from its generation at the equator to its demise to the north of 10°N.

The seasonal evolution of the SSS fronts in the Indian Ocean shows also a similar migration pattern, but in a southwest direction and having about 12 month duration. The existence of two fronts in December suggests that the one located northeast of Madagascar around 18°S is the one that formed near 5°S about a year ago. The southwest Pacific under the SPCZ encounters, however, only one front per month throughout the year, which is very different from the pattern found in three other basins. The seasonal variation in the location and magnitude of the SSS fronts is also relatively weak. The front is marginally stronger and closer to the equator in December–January compared to its condition in August–October.

The seasonal evolution of the Argo subsurface structures was examined at selected meridians in all three basins. Marked seasonal changes in the location, strength, and depth of the low-salinity cells are noted. Two meridional sections are analyzed here (Figures 7a and 7b). Along the meridional section in the central Pacific at 140°W (Figure 7a), two shallow low-salinity (or fresh) cells are observed in April, with one centered at 5°N and the other centered at 12°N. The near-equatorial fresh cell is weak and shallow. In the subsequent months, however, this cell strengthens, deepens, migrates, and eventually evolves into the cell that is displaced at 12°N in the coming April. Throughout the year, the near-surface low-salinity structure is in good correspondence with the SSS front structure (Figure 6a), with the exception of February. The surface and subsurface structures do not match exactly in February, as the surface shows two SSS fronts but the subsurface has only one fresh cell. This is unlike the case in April when the two SSS fronts are paired perfectly with

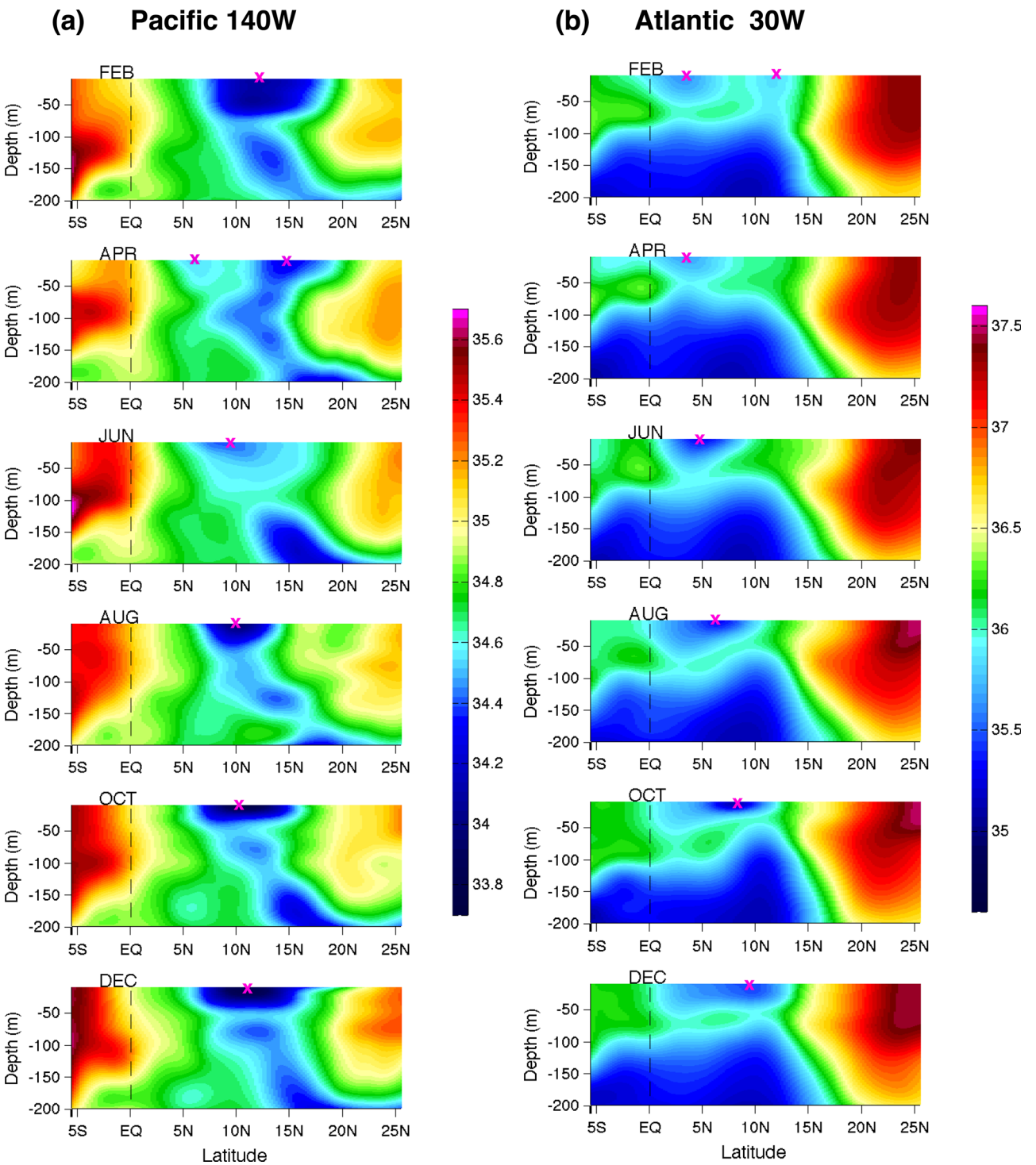

Figure 7. Bimonthly evolution of the meridional salinity sections (25°S–25°N) in the upper 200 m at (a) 140°W and (b) 30°W. The magenta cross "x" at the surface denotes the *Smin* location.

the two fresh cells in the upper 30 m. One possible explanation of missing the subsurface signature of the SSS front is the difference in the measurement depth between Aquarius and Argo. The topmost layer of the Argo gridded product in use is at the depth of 10 m below the sea surface [*Hosoda et al.*, 2010], while the Aquarius measurements are taken within the microwave penetration depth of ~1 cm [*Lagerloef et al.*,

2008; *Yu*, 2010]. If the SSS front is associated with a fresh cell that is shallower than 10 m, it is highly likely that the subsurface measurements at 10 m will not be able to capture it. The near-equatorial SSS front is more intense in April than in February, which indicates that the fresh cell is likely very shallow at its initial formation stage.

The meridional subsurface section in the central Atlantic at 30°W (Figure 7b) provides an additional example of the coupling between the surface and subsurface throughout the year. In February, the surface and subsurface are coherent in depicting the presence of a two fresh-cell pattern in the upper 30 m. The fresh cell centered at 3°N is obviously stronger than the one displaced at 12°N, which is consistent with the strength of the SSS fronts. The near-equatorial cell grows and shifts northward in the subsequent months, while the northern cell fades away within the next 2–3 months. In April, there is no signature of the northern front in the subsurface—maybe the fresh cell associated with the weak front is too shallow to reach down to the 10 m depth.

4.3. Contrast in Seasonal Movement Between the *Pmax* and *Smin* Locations

The locations of *Smin* and *Pmax* for each calendar month are compiled for the four basins (Figures 8a–8d) to help obtain a complete characterization of the seasonal migration pattern of the SMZ in each basin. The months are color coded, with the warm colors designated for October–March and the cool colors for April–September. In the north tropical Pacific (Figure 8a), the seasonal evolution of the *Pmax* locations shows a clear north/south migration, being close to the equator from December to April and at its northernmost positions between July and October. By comparison, the seasonal movement of the *Smin* locations has three distinct features. First, the presence of two *Smin* location lines occurs between January and May. One is shorter, located in the eastern equatorial region, and the other is basin scale, located in the north between 8°N and 12°N. For the remaining months, there is only one basin-scale *Smin* location line. Second, the meridional extent of the *Smin* locations is wider than that of the *Pmax* locations. The former ranges from 3°N to 15°N while the latter between 3°N and 10°N. Lastly, the *Smin* locations are in close proximity to the *Pmax* locations from June to October.

The seasonal movement of the *Smin* locations in the north tropical Atlantic (Figure 8b) shows the same three features: two *Smin* location lines in the months when the ITCZ is near the equator, the collocation with *Pmax* in the months when the ITCZ is situated in the north, and further northward migration latitudes than the ITCZ. In the south tropical Indian Ocean (Figure 8c), the ITCZ is closest to the equator during July to December, and the existence of two *Smin* location lines occurs from November to December. On the other hands, the seasonal migration of the *Smin* location lines in the southwest tropical Pacific (Figure 8d) is small and rather different from the three other basins. The *Smin* is displaced closer to the equator compared to its locations in the other months when the *Pmax* is at the southernmost position in April.

Zonal averages of the *Smin* and *Pmax* monthly location lines are constructed for all the four basins (Figures 9a–9d). Since the fronts in the north tropical Pacific and Atlantic can persist about 15–16 months, two climatological years are used in the plots to make the migration patterns to be perceived more easily. Remarkably, the monotonic poleward displacement of the *Smin* locations is prominently featured in all basins. It is apparent that all SMZs are sourced from the ITCZ rainfall when ITCZ is located at the near-equatorial latitudes, and these zones propagate poleward for the subsequent months until their dissipation at latitudes beyond 10°N/S. During the poleward propagation, a collocation between the *Smin* and *Pmax* is observed, but the collocation occurs at different months in different basins. For instance, the collocation takes place between June and October in the north tropical Pacific (Figure 9a), between January and April in the north tropical Atlantic (Figure 9b), between January and March in the south Indian Ocean (Figure 9c), and between November and December in the southwest Pacific (Figure 9d). The SMZ lasts about 15–16 months in the northern basins, about 11–13 months in the southern basins.

The study of *Yu* [2014] on the seasonal movement of the *Smin* locations in the north tropical Pacific identified the monotonic propagation of the *Smin* locations. However, the study did not have a full awareness of the persistence time of each front and misrepresented the propagation pattern [*Yu*, 2014, Figure 10]. The cross analysis of the SMZ in the three tropical basins in the present study has broadened the perspective and understanding, leading to an improved characterization of the low-salinity zone and its seasonal variations.

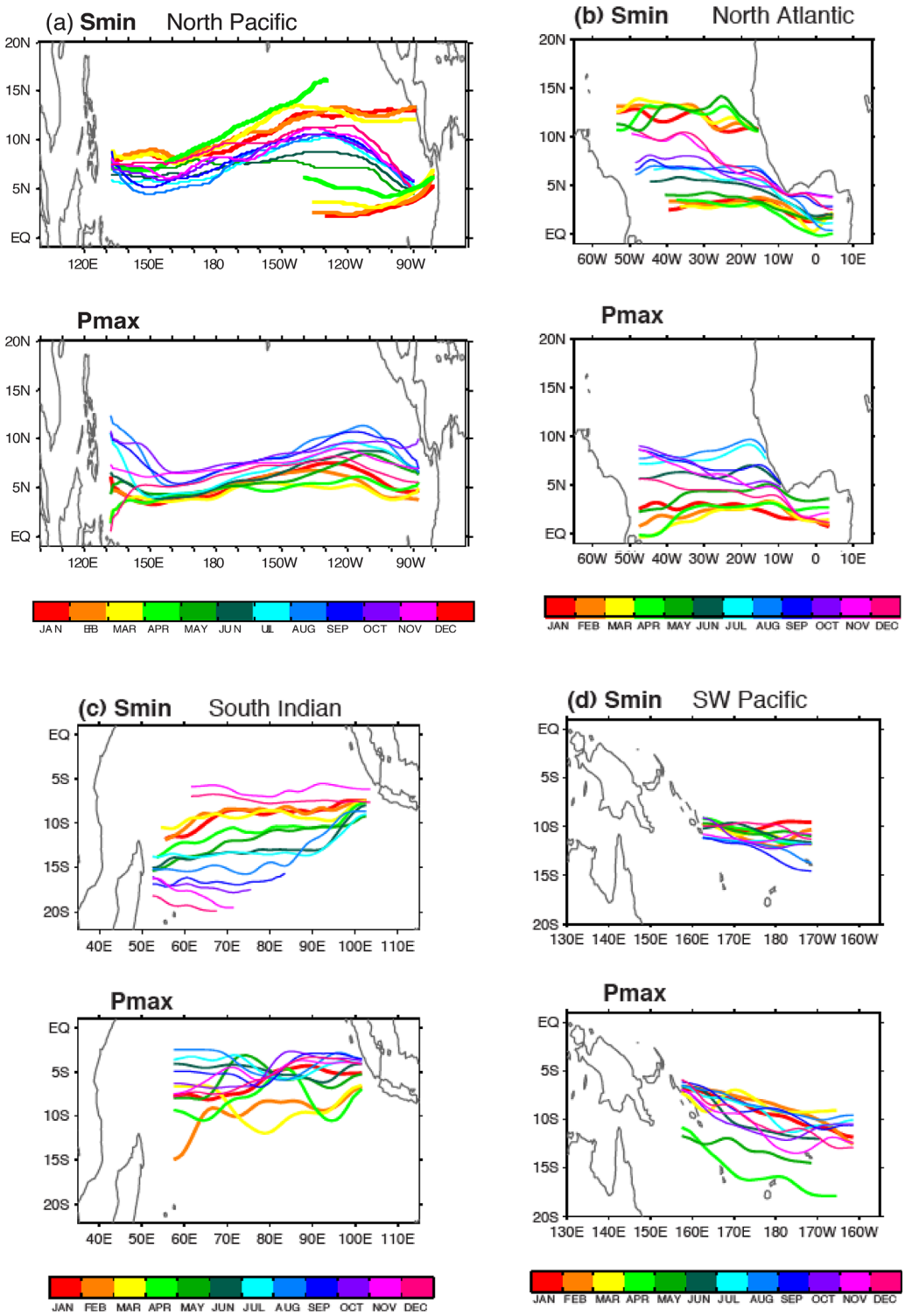

Figure 8. Seasonal displacements of the *Smin* and *Pmax* locations in (a) the north tropical Pacific, (b) the north tropical Atlantic, (c) the south Indian Ocean, and (d) the southwest tropical Pacific. In Figures 8a–8d, all the top plots are for the *Smin* locations and the bottom plots for the *Pmax* locations.

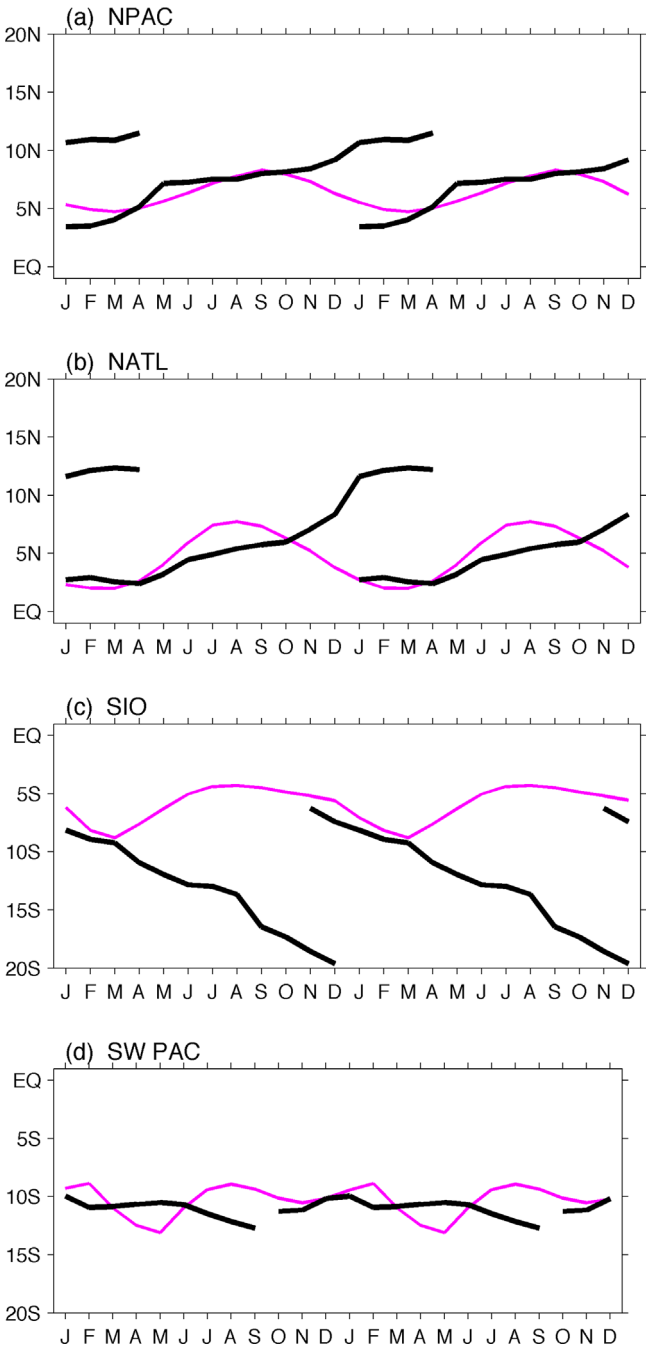

Figure 9. Zonal averages of monthly mean *Smin* (black) and *Pmax* (magenta) for the four basins: (a) the north tropical Pacific, (b) the north tropical Atlantic, (c) the south Indian Ocean, and (d) the southwest tropical Pacific.

5. Mechanisms

5.1. Ekman Transport and Convergence/Divergence

The monotonic nature in the seasonal movement of the *Smin* locations is in sharp contrast to the north/south migration of the *Pmax* locations, implying that the dominant seasonal mechanism for the SMZ cannot be the ITCZ alone. As indicated in the mixed-layer salinity budget equation (4), several oceanic processes contribute to the seasonal change of the near-surface salinity, including the salinity advection by the wind-driven Ekman currents, the salinity advection by the geostrophic currents, the vertical entrainment of subsurface salinity, and mixing.

All the terms in the salinity budget equation (4) were computed using the data described in section 2.1. The examination of the leading contribution to the salinity seasonal variability shows that the term $-\bar{\mathbf{U}}_{EK} \cdot \nabla S'$ dominates the poleward propagation of the seasonal salinity signals in all tropical basins. This is consistent with the finding of the north tropical Pacific in *Johnson et al.* [2002] and *Yu* [2014]. To see the effect more clearly, the zonal averages of monthly mean $-\bar{\mathbf{U}}_{EK} \cdot \nabla S'$ were constructed for all the basins (Figures 10a–10d). The low-salinity tendency anomalies are generated near the equatorial latitudes between January and May in the north tropical Pacific and Atlantic (Figures 10a and 10b), and subsequently carried northward away from the equator. During the northward displacement in the Pacific, a period of quasi-stationary state occurs between August and December, during which the low-salinity anomalies tend to stay at approximately the same latitude and meanwhile are enhanced. The southward propagation of the low-salinity tendency anomalies in the southern hemisphere starts from the formation latitudes near 5°S in November–December (Figures 10c and 10d). In the south Indian Ocean, the propagation speeds up in May and the tendency anomalies are strengthened during the subsequent southward displacement. In the southwest Pacific, the freshening anomalies are transported southward at a near constant speed, although the magnitude of the anomalies is weakest among all the basins and further fades away beyond 12°S.

The speed at which the tendency anomalies propagate was computed for all the four patterns. The propagation speed is ~3.4 km d^{-1} in the Pacific and ~3.6 km d^{-1} in the Atlantic—that is to say, on average, the

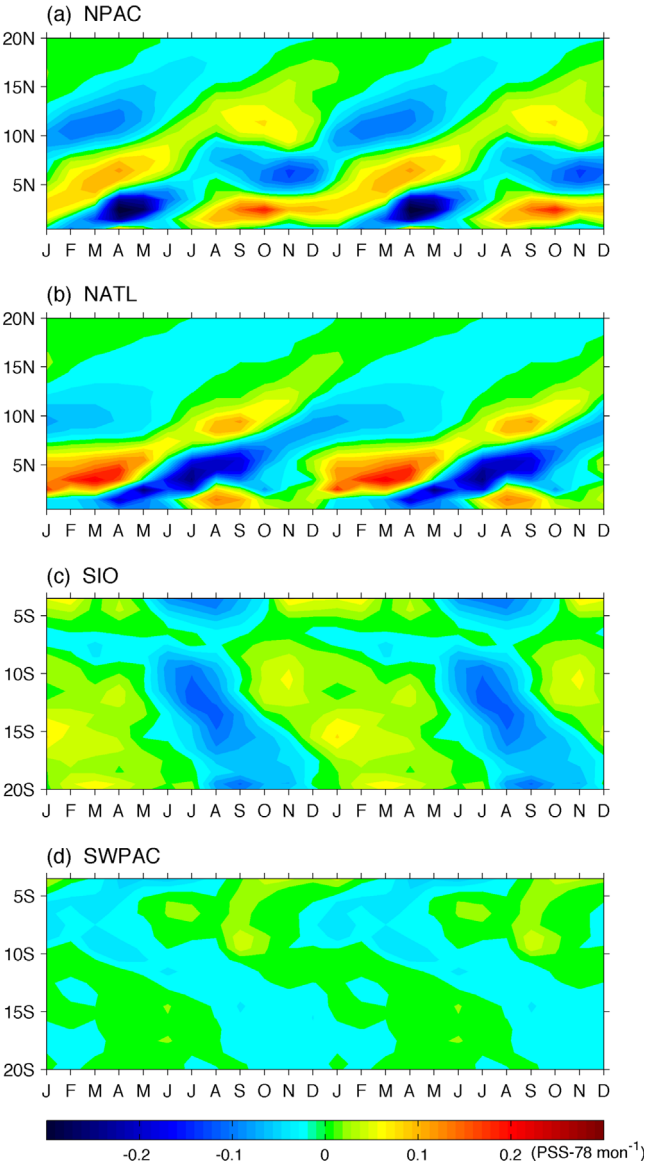

Figure 10. Zonal averages of monthly salinity advection by Ekman mean transport ($-\bar{\mathbf{U}}_{EK} \cdot \nabla S'$) for the four basins: (a) the north tropical Pacific, (b) the north tropical Atlantic, (c) the south Indian Ocean, and (d) the southwest tropical Pacific. Positive (negative) anomalies denote advection of saltier (fresher) surface waters.

low-salinity signals are being transported ~3.5 km northward every day. In the south Indian Ocean, the propagation is slower, at ~ 2.2 km d^{-1}, between November and April, and faster, at ~ 6.2 km d^{-1}, between May and October. In the southwest Pacific, although the anomalies are weak, they are propagated at a speed of ~3.6 km d^{-1}, which is comparable to the speed in the north Pacific and Atlantic. Apparently, the low-salinity signals in all the tropical basins are highly transient.

The tropical oceans within 25°S–25°N are subject to the trade winds that blow persistently toward the southwest, north of convergence zones, and toward the northwest, south of convergence zones. Because of the Coriolis effect (equation (2)), the Ekman transport from the trade winds is deflected to the right north of the equator and to the left south of the equator (Figure 11a). Therefore, the Ekman transport is poleward and westward in both hemispheres, which then drives the seasonal displacement of the *Smin* locations poleward and westward. Fundamentally, it is the trade wind system that governs the seasonal movement of the SMZ.

Ekman transport converges in some regions and diverges in the others as a result of the spatial variations of the trade winds. The convergence causes Ekman pumping or downwelling (defined as $W_{EK} < 0$; see equation (3)), which pushes the surface waters into the subsurface layers. Conversely, the divergence induces Ekman suction or upwelling ($W_{EK} > 0$), which draws the subsurface waters to the surface. *Yu* [2014] showed that the SMZ in the north tropical Pacific is formed by Ekman convergence of the rain-freshened surface waters. This mechanism applies to the SMZ in all tropical basins. The annual-mean field of zonal and meridional Ekman salinity divergence (i.e., $u_{EK} \cdot \partial S/\partial x$ and $v_{EK} \cdot \partial S/\partial y$) is shown in Figures 11b and 11c. The zonal Ekman divergence (Figure 11b) is generally weak and noisy, except for some organized convergence (negative) in the eastern Pacific north of the equator, the Amazon River outflow plume, and the Bay of Bengal. By comparison, the meridional Ekman divergence (Figure 11c) is much stronger and well structured. In the north tropical Pacific and Atlantic Oceans, there is a band of strong Ekman convergence (negative) between the equator and up to 4–10°N and a band of Ekman divergence (positive) on its north. In the southwest Pacific west of 150°W, a band of Ekman convergence appears between 2°S and 10°S. In the tropical south Indian Ocean, there is a band of weak Ekman convergence between 5°S and 12°S. The divergence patterns in Figures 11b and 11c are consistent with the study of *Johnson et al.* [2002] that the meridional salinity divergence by Ekman flow crossing the generally east-west isohalines is the dominant term.

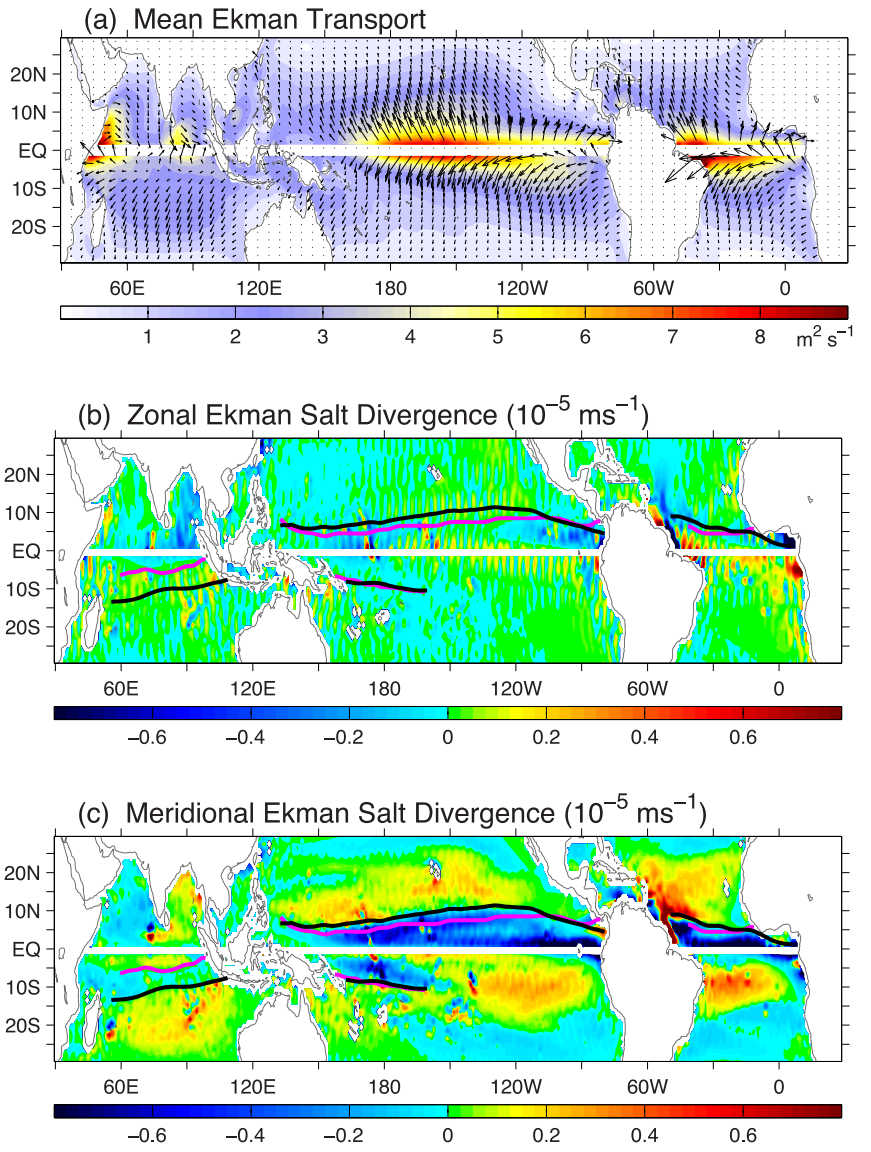

Figure 11. (a) Mean Ekman transport (U_{EK}, V_{EK}) and magnitude, (b) zonal Ekman salt divergence, and (c) Meridional Ekman divergence. In Figures 11b and 11c, negative values denote Ekman convergence (downward) and positive values Ekman divergence (upward). The *Smin* (thick black) and *Pmax* (thick magenta) are superimposed.

Superimposing the *Pmax* and *Smin* locations onto the Ekman divergence (Figures 11b and 11c) brings out one striking feature: the *Smin* location is determined by the location of the meridional Ekman convergence. The *Smin* is aligned on the northern edge of the meridional convergence zone in the north tropical Pacific and Atlantic Oceans, and on the southern edge of the meridional convergence zone in the south tropical Indian Ocean and the southwest Pacific. Compared to the *Smin* location, the *Pmax* is displaced slightly equatorward and is within the Ekman convergence zone in all the basins, except for the southwest Pacific where the *Pmax* and *Smin* are both on the southern edge of the convergence zone.

5.2. Roles of Ekman Convergence and ITCZ Rainfall

To delineate the relationship between the *Smin* location, the *Pmax* location, and the Ekman convergence zone, the bimonthly evolution of the salinity anomaly advection by mean Ekman transport is shown (Figure 12). The pattern in the north tropical Pacific and Atlantic is characterized by three zonal bands with alternating signs. Take the North Pacific as an example. In February, a weak and very narrow band of Ekman convergence (negative anomalies) appears slightly north of the equator. By April, this band of Ekman convergence

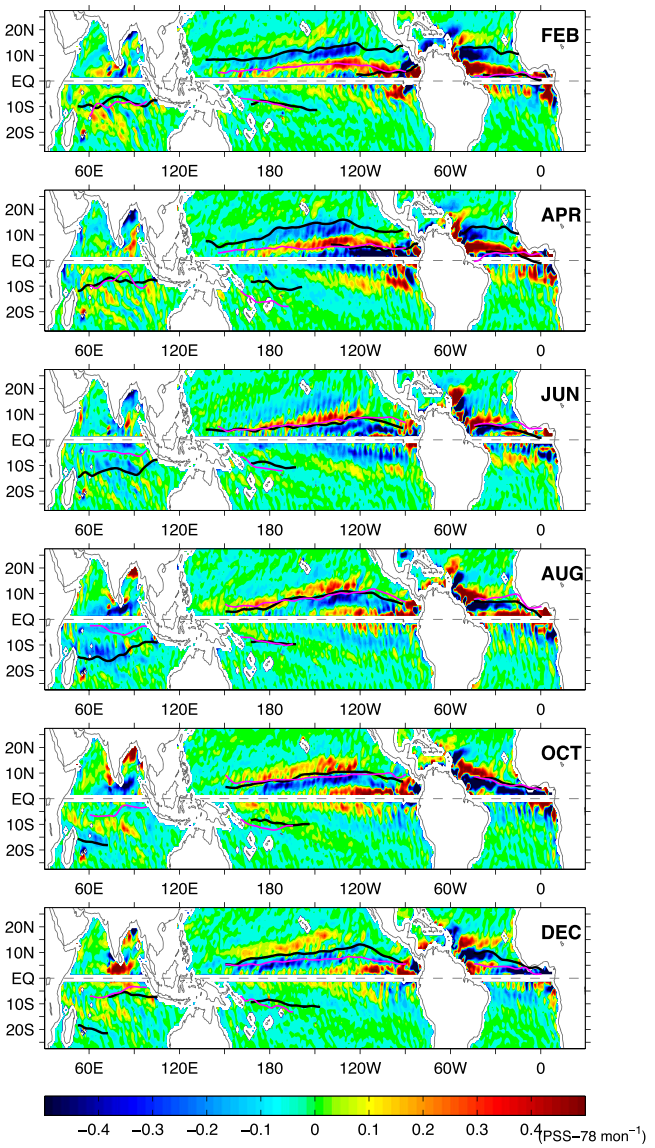

Figure 12. Bimonthly evolution of salinity advection by Ekman mean transport ($-\bar{\mathbf{U}}_{EK} \cdot \nabla S'$) from (top) February to (bottom) December. Positive (negative) anomalies denote advection of saltier (fresher) surface waters. The *Smin* (black) and *Pmax* (magenta) location lines are superimposed.

has strengthened and expanded. Meanwhile, it also overlaps with the ITCZ rainfall since February–April is a time of the year that the ITCZ rain band is closest to the equator (Figures 9a and 9b). Thus, the ITCZ-freshened surface waters are pushed into the subsurface in the Ekman convergence zone, leading to the formation of a SMZ near the equator. Here two collocation relationships can be identified. First, the *Smin* collocates with the *Pmax* at ~3°N–5°N (Figure 12). Second, the SSS fronts (Figure 6) collocate with the Ekman convergence zone between the equator and 5°N (Figure 12). The evidence sheds some insight into how a SMZ is generated at the near-equatorial latitudes during the winter season when the ITCZ is displaced near the equator.

In April, there is a second band of Ekman convergence between 5°N and 12°N in the north Pacific and Atlantic. With the ITCZ located near the equator, this band of Ekman salinity convergence is not subject to direct rainfall influence. However, one still sees the alignment of the *Smin* location on the northern edge of the convergence (Figure 12) and a SSS front collocating with the convergence zone (Figure 6). This is an indication that the Ekman convergence maintains the SMZ. One also sees that the magnitude of the SSS front is weaker than the one near the equator, suggesting that with no direct influence of the ITCZ rainfall, the converged surface waters are saltier than those near the equator and hence, the SSS front at 10°N is weaker (Figure 6) and the associated SMZ is also weaker (Figures 7a and 7b).

During the seasonal northward shift of the trade system from February to August, the *Smin* and *Pmax* locations stay close to each other and move northward in tandem with the northward progression of the Ekman convergence zone from the its near-equatorial position. When the ITCZ reaches the northernmost latitude at ~10°N in August, the harmony begins to break down. Ekman divergence (positive) develops in the near-equatorial region and dominates from August to December (Figure 12). During this time, although the ITCZ is on the way moving toward the equator, no SMZ is formed near the equator.

Throughout the seasonal transitions, the *Smin* locations in the north Pacific and Atlantic remain on the northern edges of the convergence anomaly bands. The anomalies in the southwest Pacific and south Indian Ocean generally weak between December and May. The alignment of the *Smin* on the southern edges of the convergence bands is evidenced only for those months (June–October) when anomalies are sufficiently large.

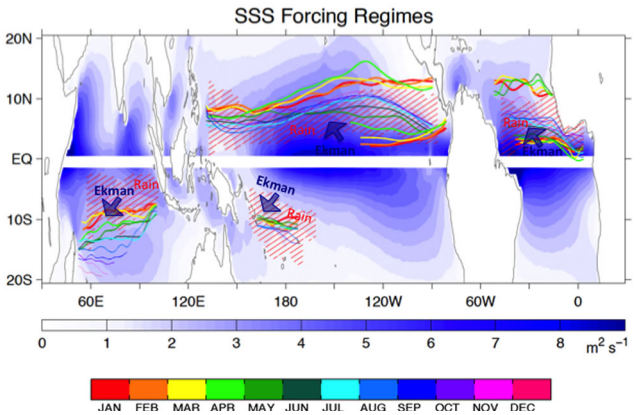

Figure 13. Schematic diagram depicting the *Smin* location lines (color-coded by month) with respect to two forcing regimes: the trade wind Ekman transport (the background blue shading) and the ITCZ rain (denoted by the *Pmax* migration latitudes in the red hatch-filled region).

6. Summary and Discussions

Low-salinity surface waters in the tropical open ocean are known to result from the intense and persistent ITCZ rainfall. It is evidenced from the Aquarius and Argo observations that the surface salinity minima are organized not along the ITCZ maximum rainfall (Figure 1) but along the poleward edges of the SSS fronts (Figure 2). In particular, the SSS fronts are a surface manifestation of the salinity-minimum zone of 50–80 m deep (Figures 3 and 4). By utilizing the satellite-derived surface forcing products, we conducted a near-surface salinity budget analysis and provided a detailed description of the three issues: the mechanism that supports the connection between salinity minima and the SSS front, the characteristics of the seasonal distribution of the salinity minima, and the relative roles of the ITCZ forcing versus the trade wind Ekman transport in seasonal dynamics of the tropical salinity minima. The analysis was made to the three tropical basins, and the following main inferences can be drawn from the study.

1. On the seasonal time scales, the rain-freshened surface waters are converged into the subsurface layers by Ekman pumping, leading to a formation of SMZ in the upper 80 m (Figure 7) across the entire tropical ocean (Figures 11 and 12). Collocation between the Ekman convergence zones and the SSS fronts is evidenced, supporting the conventional concept that a salinity front is the boundary of two surface water masses, which are the ITCZ-freshened surface waters and the ambient saltier surface waters in this case.
2. The location lines of *Smin* and *Pmax* were used to represent the respective central position of the SMZ and the ITCZ rainfall. There is no direct relationship between *Smin* and *Pmax*. In the north tropical Pacific, the *Smin* and *Pmax* are aligned together in August at the northernmost location of the ITCZ but stay apart in February, during the time the *Pmax* is at its near-equatorial position while the *Smin* is about 5° farther north from its position in August (Figure 5). The difference in the seasonal migration pattern characterizes the major difference between the SMZ and the ITCZ.
3. In contrast to the seasonal north/south migration of the ITCZ, the SMZ is marked by seasonal monotonic poleward propagation at an average speed of ~3.5 km d^{-1} from its generation at the near-equatorial latitudes until its dissipation beyond 15°N/S (Figures 6, 8, and 9). The poleward propagation persists about 12 months in the south tropical Indian Ocean and 15–16 months in the north tropical Pacific and Atlantic. The persistence of 1 year and longer leads to the coexistence of two SMZs during December–May. The newly formed SMZ is located near the equator (Figures 7 and 8), coinciding with the near-equatorial position of the ITCZ. The SMZ that is formed in the previous year is located near the latitudes of 10–15° poleward after 1 year's propagation.

In summary, the leading forcing for the seasonal formation and spatial distribution of the intertropical SMZ is the oceanic Ekman transport and convergence in response to the trade winds, with the ITCZ rainfall being the source of surface freshening (Figure 11). In the north Pacific and Atlantic, the SMZ is formed at the near-equatorial latitudes during February–April when the equatorward displaced ITCZ collocates with an Ekman salinity convergence zone near the equator (Figure 12). The SMZ is intensified and deepened during April–August when the Ekman convergence zone moves northward in tandem with the ITCZ rainfall. The harmony starts to break down after August when the ITCZ begins its annual retreat toward the equator. While the SMZ continues its northward progression by the Ekman convergence, the lack of the direct influence of the ITCZ makes the surface waters saltier and the SMZ weaker. To summarize the forcing influence of the Ekman transport and rainfall on the seasonal generation and variations of the SMZ, a schematic diagram is drawn to depict the influence regime of each forcing (Figure 13). In this framework, the coupling of the

SSS front with a subsurface zone by Ekman convergence sustains the structure of the low-salinity anomalies in the zone, and meanwhile makes the SMZ subject to the ocean circulation in response to the trade winds.

Salinity is a conservative tracer. Once salinity anomalies are generated by the freshwater flux (i.e., evaporation (E), precipitation (P), and river runoff (R)), the properties are not changed when circulating around with ocean currents [*Dickson et al*., 1988], except subject to mixing and diffusion. One distinct feature of the SMZ is the possession of closed isohaline contours (Figures 3 and 4), which allows one to define an isohaline surface that bounds the low-salinity waters sourced from the ITCZ by a closed volume. The salinity budget can be formulated for this choice of control volume that does not have the advective contribution in it, thus relating the surface freshwater fluxes directly to the tendency of the salinity volume and the mixing processes across the bounding surface. The isohaline salinity budget analysis is in a similar vein to the one used in studying the isothermal heat budget of the tropical warm water pools [*Niiler and Stevenson*, 1982; *Toole et al*., 2004; *Enfield and Lee*, 2005; *Song and Yu*, 2013], and has recently been applied to the North Atlantic salinity maximum by *Bryan and Bachman* [2015]. This approach is different from the commonly used mixed-layer salinity budget analysis [e.g., *Johnson et al*., 2002; *Yu*, 2011; *Hasson et al*., 2013] that shows the important contribution of the advective divergence terms to seasonal salinity variability in the tropical ocean and the consequent challenges for determining the surface freshwater fluxes from the near-surface salinity observations. The approach of the isohaline-bounded salinity budget of the SMZ is a Lagrangian approach, which allows avoiding the advection divergence contribution that is usually large in Eulerian approach. This could open up a new strategy for using the SMZ as an ocean rain-gauge for tracking the tropical water cycle. Work is being continued to that end.

Acknowledgments

The study was supported by the NASA Ocean Salinity Science Team (OSST) under grant NNX12AG93G. Support from the NOAA Office of Climate Observation (OCO) under grant NA09OAR4320129 and NASA Ocean Vector Wind Science Team (OVWST) under grant NNA10AO86G in developing OAFlux evaporation and surface wind stress used in the study is gratefully acknowledged. Shirley Cabral-McDonald proofread the manuscript. The OAFlux evaporation and wind stress can be downloaded from http://oaflux.whoi.edu. The Aquarius CAP SSS products were from JPL PO.DAAC ftp://podaac.jpl.nasa.gov/allData/aquarius/L2/CAPv2/. The Argo-based gridded salinity and temperature fields were from the JAMSTEC Argo group ftp://ftp2.jamstec.go.jp/pub/argo/MOAA_GPV/Glb_PRS/OI/. The altimeter products were produced by Ssalto/Duacs and distributed by AVISO, with support from Cnes (http://www.aviso.oceanobs.com/duacs/). The mean dynamic ocean topography was from http://apdrc.soest.hawaii.edu/projects/DOT/. The TRMM precipitation 3B43 products were from ftp://disc2.nascom.nasa.gov/data/s4pa/TRMM_L3/TRMM_3B43/.

References

Adler, R. F., et al. (2003), The Version-2 Global Precipitation Climatology Project (GPCP) monthly precipitation analysis (1979-present), *J. Hydrometeorol.*, *4*, 1147–1167.

Allen, M. R., and W. J. Ingram (2002), Constraints on future changes in climate and the hydrologic cycle, *Nature*, *419*(6903), 224–232.

Alory, G., C. Maes, T. Delcroix, N. Reul, and S. Illig (2012), Seasonal dynamics of sea surface salinity off Panama: The far eastern Pacific fresh pool, *J. Geophys. Res.*, *117*, C04028, doi:10.1029/2011JC007802.

Asher, W. E., A. T. Jessup, R. Branch, and D. Clark (2014), Observations of rain-induced near-surface salinity anomalies, *J. Geophys. Res. Oceans*, *119*, 5483–5500, doi:10.1002/2014JC009954.

Betts, A. K., and W. L. Ridgway (1989), Climatic equilibrium of the atmospheric convective boundary layer over a tropical ocean, *J. Atmos. Sci.*, *46*, 2621–2641.

Brainerd, K. E., and M. C. Gregg (1997), Turbulence and stratification on the Tropical Ocean-Global Atmosphere-Coupled Ocean-Atmosphere Response Experiment microstructure pilot cruise, *J. Geophys. Res.*, *102*(C5), 10,437–10,455.

Bryan, F., and S. Bachman (2015), Isohaline salinity budget of the north Atlantic salinity maximum, *J. Phys. Oceanogr.*, *45*, 724–736, doi:10.1175/JPO-D-14-0172.1.

Da-Allada, C. Y., G. Alory, Y. du Penhoat, E. Kestenare, F. Durand, and N. M. Hounkonnou (2013), Seasonal mixed-layer salinity balance in the tropical Atlantic Ocean: Mean state and seasonal cycle, *J. Geophys. Res. Oceans*, *118*, 332–345, doi:10.1029/2012JC008357.

de Boyer Montégut, C., G. Madec, A. S. Fischer, A. Lazar, and D. Iudicone (2004), Mixed layer depth over the global ocean: An examination of profile data and a profile-based climatology, *J. Geophys. Res.*, *109*, C12003, doi:10.1029/2004JC002378.

Delcroix, T., and C. Henin (1991), Seasonal and interannual variations of sea-surface salinity in the tropical Pacific Ocean, *J. Geophys. Res.*, *96*(C12), 22,135–22,150.

Delcroix, T., and J. Picaut (1998), Zonal displacement of the western equatorial Pacific "fresh pool," *J. Geophys. Res.*, *103*(C1), 1087–1098, doi:10.1029/97JC01912.

Delcroix, T., C. Henin, V. Porte, and P. Arkin (1996), Precipitation and sea surface salinity in the tropical Pacific, *Deep Sea Res., Part I*, *43*, 1123–1141.

Delcroix, T., G. Alory, S. Cravatte, T. Corrège, and M. McPhaden (2011), A gridded sea surface salinity data set for the tropical Pacific with sample applications (1950–2008), *Deep Sea Res., Part I*, *58*, 38–48, doi:10.1016/j.dsr.2010.11.002.

Dickson, R. R., J. Meincke, S. A. Malmberg, and A. J. Lee (1988), The "great salinity anomaly" in the northern North Atlantic 1968–1982, *Prog. Oceanogr.*, *20*(2), 103–151.

Donguy, J. R., and C. Henin (1980), Surface conditions in the eastern equatorial Pacific related to the intertropical convergence zone of the winds, *Deep Sea Res., Part A*, *27*, 693–714.

Elliott, G. W. (1974), Precipitation signatures in sea-surface-layer conditions during BOMEX, *J. Phys. Oceanogr.*, *4*, 498–501.

Enfield, D. B., and S.-K. Lee (2005), The heat balance of the Western Hemisphere warm pool, *J. Clim.*, *18*, 2662–2681, doi:10.1175/JCLI3427.1.

Fiedler, P. C., and L. D. Talley (2006), Hydrography of the eastern tropical Pacific: A review, *Prog. Oceanogr.*, *69*(2), 143–180, doi:10.1016/j.pocean.2006.03.008.

Font, J., A., Camps, A. Borges, M. Martín-Neira, J. Boutin, N. Reul, Y. H. Kerr, A. Hahne, and S. Mecklenburg (2010), SMOS: The challenging sea surface salinity measurement from space, *Proc. IEEE*, *98*(5), 649–665, doi:10.1109/JPROC.2009.2033096.

Godfrey, J. S., and E. J. Lindstrom (1989), The heat budget of the equatorial western Pacific surface mixed layer, *J. Geophys. Res.*, *94*(C6), 8007–8017, doi:10.1029/JC094iC06p08007.

Gouriou, Y., and T. Delcroix (2002), Seasonal and ENSO variations of sea surface salinity and temperature in the South Pacific Convergence Zone during 1976–2000, *J. Geophys. Res.*, *107*(C12), 8011, doi:10.1029/2001JC000830.

Hasson, A., T. Delcroix, J. Boutin, R. Dussin, and J. Ballabrera-Poy (2014), Analyzing the 2010–2011 La Niña signature in the tropical Pacific sea surface salinity using in situ data, SMOS observations, and a numerical simulation, *J. Geophys. Res. Oceans*, *119*, 3855–3867, doi:10.1002/2013JC009388.

Hasson, A. E. A., T. Delcroix, and R. Dussin (2013), An assessment of the mixed layer salinity budget in the tropical Pacific Ocean: Observations and modelling (1990–2009), *Ocean Dyn.*, *63*(2–3), 179–194, doi:10.1007/s10236-013-0596-2.

Hastenrath, S., and P. J. Lamb (1978), On the dynamics and climatology of surface flow over the equatorial oceans, *Tellus*, *30*, 436–448.

Hoffman, G. F., D. T. Bolvin, E. J. Nelkin, D. B. Wolff, R. F. Adler, G. J. Gu, Y. Hong, K. P. Bowman, and E. F. Stocker (2007), The TRMM Multisatellite Precipitation Analysis (TMPA): Quasi-global, multiyear, combined-sensor precipitation estimates at fine scales, *J. Hydrometeorol.*, *8*, 38–55.

Hosoda, S., T. Ohira, K. Sato, and T. Suga (2010), Improved description of global mixed-layer depth using Argo profiling floats, *J. Oceanogr.*, *66*, 773–787.

Johnson, E. S., G. S. E. Lagerloef, J. T. Gunn, and F. Bonjean (2002), Surface salinity advection in the tropical oceans compared with atmospheric freshwater forcing: A trial balance, *J. Geophys. Res.*, *107*(C12), 8014, doi:10.1029/2001JC001122.

Johnson, G. C., S. Schmidtko, and J. M. Lyman (2012), Relative contributions of temperature and salinity to seasonal mixed layer density changes and horizontal density gradients, *J. Geophys. Res.*, *117*, C04015, doi:10.1029/2011JC007651.

Kao, H. Y., and G. S. Lagerloef (2015), Salinity fronts in the tropical Pacific Ocean, *J. Geophys. Res. Oceans*, *120*, 1096–1106, doi:10.1002/2014JC010114.

Kraus, E. B., and J. S. Turner (1967), A one-dimensional model of the seasonal thermocline II. The general theory and its consequences, *Tellus*, *19*(1), 98–106.

Lagerloef, G., et al. (2008), The Aquarius/SAC-D Mission: Designed to meet the salinity remote-sensing challenge, *Oceanography*, *21*(1), 68–81, doi.10.5670/oceanog.2008.68.

Lukas, R. (1990), The role of salinity in the dynamics and thermodynamics of the western Pacific warm pool, in *Proceedings of the International TOGA Scientific Conference*, Honolulu, HI, July 16–20, World Climate Research Programme Publication, WCRP-43, pp. 73–81, Geneva, Switzerland.

Lukas, R., and E. J. Lindstrom (1991), The mixed layer of the western equatorial Pacific Ocean, *J. Geophys. Res.*, *96*(S01), 3343–3358.

Maes, C., K. Ando, T. Delcroix, W. S. Kessler, M. J. McPhaden, and D. Roemmich (2006), Observed correlation of surface salinity, temperature and barrier layer at the eastern edge of the western Pacific warm pool, *Geophys. Res. Lett.*, *33*, L06601, doi:10.1029/2005GL024772.

Maximenko, N. A., P. Niiler, M.-H. Rio, O. Melnichenko, L. Centurioni, D. Chambers, V. Zlotnicki, and B. Galperin (2009), Mean dynamic topography of the ocean derived from satellite and drifting buoy data using three different techniques, *J. Atmos. Oceanic Technol.*, *26*(9), 1910–1919.

Mignot, J., and C. Frankignoul (2003), On the interannual variability of surface salinity in the Atlantic, *Clim. Dyn.*, *20*, 555–565.

Niiler, P., and J. Stevenson (1982), The heat budget of tropical ocean warm-water pools, *J. Mar. Res.*, *40*, 465–480.

Niiler, P. P., and E. B. Kraus (1977), One-dimensional models, in *Modeling and Prediction of the Upper Layers of the Ocean*, edited by E. B. Kraus, pp. 143–172, Pergamon, N. Y.

Niiler, P. P., N. A. Maximenko, and J. C. McWilliams (2003), Dynamically balanced absolute sea level of the global ocean derived from near-surface velocity observations, *Geophys. Res. Lett.*, *30*(22), 2164, doi:10.1029/2003GL018628.

Qu, T., H. Mitsudera, and T. Yamagata (2000), Intrusion of the North Pacific waters into the South China Sea, *J. Geophys. Res.*, *105*(C3), 6415–6424.

Qu, T., S. Gao, and R. A. Fine (2013), Subduction of south Pacific tropical water and its equatorward pathways as shown by a simulated passive tracer, *J. Phys. Oceanogr.*, *43*, 1551–1565, doi:10.1175/JPO-D-12-0180.1.

Rao, R. R., and R. Sivakumar (2003), Seasonal variability of sea surface salinity and salt budget of the mixed layer of the north Indian Ocean, *J. Geophys. Res.*, *108*(C1), 3009, doi:10.1029/2001JC000907.

Reul, N., B. Chapron, T. Lee, C. Donlon, J. Boutin, and G. Alory (2014), Sea surface salinity structure of the meandering Gulf Stream revealed by SMOS sensor, *Geophys. Res. Lett.*, *41*, 3141–3148, doi:10.1002/2014GL059215.

Roemmich, D., G. C. Johnson, S. Riser, R. Davis, J. Gilson, W. B. Owens, S. L. Garzoli, C. Schmid, and M. Ignaszewski (2009), The Argo Program: Observing the global oceans with profiling floats, *Oceanography*, *22*, 34–43, doi:10.5670/oceanog.2009.36.

Short, D. A., P. A. Kucera, B. S. Ferrier, J. C. Gerlach, S. A. Rutledge, and O. W. Thiele (1997), Shipboard radar rainfall patterns within the TOGA COARE IFA, *Bull. Am. Meteorol. Soc.*, *78*, 2817–2836.

Simpson, J. E., and R. E. Britter (1979), The dynamics of the head of a gravity current advancing over a horizontal surface, *J. Fluid Mech.*, *94*, 477–495.

Soloviev, A., and R. Lukas (1997), Sharp frontal interfaces in the near-surface layer of the ocean in the Western Equatorial Pacific warm pool, *J. Phys. Oceanogr.*, *27*, 999–1017, doi:10.1175/1520-0485(1997)027<0999:SFIITN>2.0.CO;2.

Soloviev, A., R. Lukas, and H. Matsuura (2002), Sharp frontal interfaces in the near-surface layer of the tropical ocean, *J. Mar. Syst.*, *37*(1), 47–68.

Song, X., and L. Yu (2013), How much net surface heat flux should go into the western Pacific warm pool?, *J. Geophys. Res. Oceans*, *118*, 3569–3585, doi:10.1002/jgrc.20246.

Toole, J. M., H.-M. Zhang, and M. J. Caruso (2004), Time-dependent internal energy budgets of the tropical warm water pools, *J. Clim.*, *17*, 1398–1410, doi:10.1175/1520-0442(2004)017<1398:TIEBOT>2.0.CO;2.

Vialard, J., and P. Delecluse (1998), An OGCM study for the TOGA decade. Part I: Role of salinity in the physics of the western Pacific fresh pool, *J. Phys. Oceanogr.*, *28*(6), 1071–1088.

Vincent, D. G. (1994), The South Pacific convergence zone (SPCZ): A review, *Mon. Weather Rev.*, *122*(9), 1949–1970.

Waliser, D. E., and C. Gautier (1993), A global climatology of the ITCZ, *J. Clim.*, *6*, 2162–2174.

Wijesekera, H. W., C. A. Paulson, and A. Huyer (1999), The effect of rainfall on the surface layer during a westerly wind burst in the western equatorial Pacific, *J. Phys. Oceanogr.*, *29*, 612–632.

Xie, P-P., and P. A. Arkin (1997), Global Precipitation: A 17-Year Monthly Analysis Based on Gauge Observations, Satellite Estimates, and Numerical Model Outputs, *Bull. Amer. Meteor. Soc.*, *78*, 2539–2558, doi:10.1175/1520-0477(1997)078<2539:GPAYMA>2.0.CO;2.

Yu, L. (2010), On surface salinity skin effect under evaporation conditions and implications for remote sensing of ocean salinity, *J. Phys. Oceanogr.*, *40*, 85–102.

Yu, L. (2011), A global relationship between the ocean water cycle and near-surface salinity, *J. Geophys. Res.*, *116*, C10025, doi:10.1029/2010JC006937.

Yu, L. (2014), Coherent evidence from Aquarius and Argo for the existence of a shallow low-salinity convergence zone beneath the Pacific ITCZ, *J. Geophys. Res. Oceans*, *119*, 7625–7644, doi:10.1002/2014JC010030.

Yu, L., and X. Jin (2014), Insights on the OAFlux ocean surface vector wind analysis merged from scatterometers and passive microwave radiometers (1987 onward), *J. Geophys. Res. Oceans*, *119*, 5244–5269, doi:10.1002/2013JC009648.

Yu, L., and R. A. Weller (2007), Objectively Analyzed air-sea heat Fluxes (OAFlux) for the global ocean, *Bull. Am. Meteorol. Soc.*, *88*(5), 527–539.

Yu, L., X. Jin, and R. Weller (2008), *Multidecade* global flux datasets from the Objectively Analyzed Air-sea Fluxes (OAFlux) Project: Latent and sensible heat fluxes, ocean evaporation, and related surface meteorological variables, *OAFlux Proj. Tech. Rep.* OA-2008-01, 64 pp., Woods Hole Oceanographic Institution, Woods Hole, Mass.

Yueh, S., W. Tang, A. Fore, A. Hayashi, Y. T. Song, and G. Lagerloef (2014), Aquarius geophysical model function and combined active passive algorithm for ocean surface salinity and wind retrieval, *J. Geophys. Res. Oceans*, *119*, 5360–5379, doi:10.1002/2014JC009939.

Zeng, L., W. Timothy Liu, H. Xue, P. Xiu, and D. Wang (2014), Freshening in the South China Sea during 2012 revealed by Aquarius and in situ data, *J. Geophys. Res. Oceans*, *119*, 8296–8314, doi:10.1002/2014JC010108.